DIRECT SURFACE PRESSURE-BASED SOURCE LOCALIZATION ON A NACA0012 AIRFOIL

Gershwin G. Ramasawmy[1], Jan W. Delfs[1], R. Ewert[1]

[1]*Institute of Aerodynamics and Flow Technology, German Aerospace Center (DLR), Lilienthalplatz 7, 38108 Braunschweig, Germany*

This contribution has been accepted based on the submitted abstract. The submitted manuscript was not reviewed and is reproduced here without edits or corrections by the conference board. Neither the EAA nor the AAA take responsibility for its contents.

Abstract

Aerodynamic source localization is conventionally performed by reconstructing acoustic source distributions from real or virtual microphone-array signals after propagation to the far field. Delfs and Ruck[1], [2] recently proposed a diffraction-filtering methodology that reconstructs the acoustically active surface pressure, and an associated surface source quantity, directly from the simulated surface pressure, thereby localizing sources without beamforming or far-field propagation. In the present work the methodology is implemented within a frequency-domain Ffowcs Williams–Hawkings (FW-H) framework and applied to wall-modelled (WMLES) large-eddy simulations of a NACA0012 airfoil at 0° and 6° angle of attack, computed with the MGLET solver [3], [4]. A mesh-convergence study first identifies a converged surface-pressure solution, from which the surface source distributions are reconstructed for both angles of attack. As an independent localization reference, conventional delay-and-sum beamforming is applied to microphone cross-spectral matrices synthesised with the in-house FW-H solver FWH-next and processed in Acoular [5], [6], using the CFD surface as a common scanning grid. The reconstructed maps identify the trailing edge as the dominant source, resolve finer spatial detail than beamforming, and preserve the radiated far-field spectrum despite suppressing the surface pressure by up to about 40 dB.

Keywords: *source localization, diffraction filtering, ffowcs williams–hawkings method, beamforming, wall-modelled les*

1. Introduction

The localization of aerodynamic sound sources is a central objective in computational aeroacoustics: it reveals the flow mechanisms responsible for acoustic radiation and guides the design of noise-reduction technologies. Acoustic analogies such as the Ffowcs Williams–Hawkings (FW-H) equation are widely used to predict far-field sound from scale-resolving CFD [7], after which the sources are usually localized by beamforming applied to measured or numerically generated microphone signals [5], [8]. Beamforming, however, operates on the propagated acoustic field and its spatial resolution is fundamentally limited by the array aperture through the point-spread function, which smears compact sources such as an airfoil trailing edge.

Delfs and Ruck [1], [2] recently introduced a diffraction-filtering methodology that derives the acoustically active surface pressure, and an associated surface source quantity, directly from the simulated surface pressure, thereby localizing sources without beamforming or far-field propagation. Rather than inferring source locations from a propagated field, the method identifies the surface regions responsible for radiation directly from the CFD solution, offering resolution set by the vortical structures rather than by the sound.

The objective of the present work is to use the method on a realistic, fully turbulent configuration: wall-modelled large-eddy simulations (WMLES) of a NACA0012 airfoil at $\alpha = 0°$ and 6°. The contribution is threefold: (i) the diffraction filter is integrated into the frequency-domain implementation of the in-house FW-H solver FWH-next and applied to WMLES surface data; (ii) a mesh-convergence study establishes the surface resolution required for a converged reconstruction; and (iii) the reconstructed source maps are compared, point-wise on an identical surface grid, with conventional delay-and-sum beamforming used as an independent localization reference.

2. Methodology

Conventional beamforming estimates source locations from microphone signals after acoustic propagation. The present method instead reconstructs the acous-

Corresponding author: *geervan.ramasawmy@dlr.de.*

tically active surface pressure directly on the FW-H surface, removing the need for far-field propagation and array processing.

2.1. Theoretical formulation

The near-field reconstruction follows the frequency-domain formulation of Delfs and Ruck [1], [2]. For a stationary rigid integration surface, and neglecting the normal pressure-gradient term, the frequency-domain FW-H boundary integral for flow at small Mach number the pressure fluctuation at some reception point $\mathbf{x}$ reads,

$$\hat{p}(\mathbf{x}) = \hat{p}_{\mathrm{f}}(\mathbf{x}) + \frac{1}{4\pi} \oint_{\partial V_B} \frac{e^{-ikr}(ikr+1)}{r^2} (\mathbf{e}_r \cdot \mathbf{n})\, \hat{p}(\boldsymbol{\xi})\, \mathrm{d}S, \tag{1}$$

where $\hat{p}$ is the complex surface pressure, $\hat{p}_{\mathrm{f}}$ the free-field pressure, k the acoustic wavenumber, $\mathbf{n}$ the outward surface normal, $\mathbf{e}_r$ the source–to–observer unit vector and $r = |\mathbf{x} - \boldsymbol{\xi}|$.

As the observer approaches the surface the boundary integral is evaluated in the Cauchy principal-value (P.V.) sense. Physically, the pressure on a rigid wall may be understood a the superposition of the incident (free-field) pressure and its mirror reflection and any diffractional part,

$$\hat{p} = \hat{p}_{\mathrm{S}} + 2\hat{p}_{\mathrm{f}}, \tag{2}$$

in which p_{f} appears doubled because of the mentioned reflection and $\hat{p}_{\mathrm{S}}$ is the acoustically active surface pressure. Rearranging removes the non-radiating free-field contribution $\hat{p}_{\mathrm{f}}$,

$$\hat{p}_{\mathrm{S}} = \hat{p} - 2\hat{p}_{\mathrm{f}}. \tag{3}$$

Combining Eqs. (1)–(3) with the principal-value jump of the double-layer integral eliminates $\hat{p}_{\mathrm{f}}$ and yields the active surface pressure directly from the total pressure,

$$\hat{p}_{\mathrm{S}}(\boldsymbol{x}) = \frac{1}{2\pi} \overset{\mathrm{P.V.}}{\oint_{\partial V_B}} \frac{e^{-ikr}(ikr+1)}{r^2} (\mathbf{e}_r \cdot \mathbf{n})\, \hat{p}(\boldsymbol{\xi})\, \mathrm{d}S. \tag{4}$$

Applying the same filter a second time defines the reconstructed surface source quantity used throughout as the localization metric,

$$\hat{q}_{\mathrm{S}}(\mathbf{x}) = \tfrac{1}{2}\hat{p}_{\mathrm{S}} - \frac{1}{4\pi} \overset{\mathrm{P.V.}}{\oint_{\partial V_B}} \frac{e^{-ikr}(ikr+1)}{r^2} (\mathbf{e}_r \cdot \mathbf{n})\, \hat{p}_{\mathrm{S}}(\boldsymbol{\xi})\, \mathrm{d}S. \tag{5}$$

In practice $\hat{p}_{\mathrm{S}}$ is obtained directly from the measured total pressure through Eq. (4); the free-field pressure is then recovered from Eq. (3) as $\hat{p}_{\mathrm{f}} = \frac{1}{2}(\hat{p} - \hat{p}_{\mathrm{S}})$.

2.2. Numerical implementation

The reconstruction was incorporated into the frequency-domain implementation of FWH-next, so that surface source reconstruction and far-field prediction operate on the same surface data. The FW-H integration surface is taken directly from the CFD surface discretization by supplying the node coordinates, outward normals and element areas to the solver. The surface pressure from the WMLES is transformed to the frequency domain and passed to the reconstruction, which evaluates complex valued $\hat{p}_{\mathrm{S}}$ and $\hat{q}_{\mathrm{S}}$ through the boundary integrals above. Because the same surface discretization is also used as the beamforming scanning grid, both methods return source distributions at identical locations, allowing a point-wise comparison without interpolation.

Table 1: Principal parameters of the WMLES (0.25 mm surface mesh).

Parameter	Value
Angle of attack (°)	0, 6
Chord length (m)	0.4
Freestream velocity (m/s)	56 (0°), 53 (6°)
Reynolds number	1.50×10^6 (0°), 1.42×10^6 (6°)
Surface mesh resolution (mm)	0.25
Surface points	900 528
Grid cells	1.86×10^8
Sampling time (s)	0.32
Time step (s)	2×10^{-6}

2.3. Large-eddy simulation

The WMLES of the NACA0012 airfoil at $\alpha = 0°$ and 6° were performed with the MGLET solver [3] utilising the Category 1 trailing edge noise test cases 1 and 3 as defined within the *Benchmark Problems for Airframe Noise Computations* (BANC) activity. Main results of this benchmark activity have been reported in Herr et al. [9], [10]. Further results of the numerical setup can be found in [11]. MGLET makes use of a Hydrodynamic/Acoustic Splitting (HAS) formulation that separates the pressure into hydrodynamic and acoustic components [12]; the resolved surface pressure is used as input to both the surface reconstruction and the FWH-next. Three surface resolutions (1.0, 0.5 and 0.25 mm) were examined for $\alpha = 0°$. On the basis of the resulting mesh-convergence study (Sec. 3.1), the 0.25 mm mesh was retained for the comparison of the two angles of attack. The principal parameters are listed in Table 1. All simulations employed the same hierarchical Cartesian multi-domain mesh topology with local near-wall refinement. For the mesh-sensitivity study, only the surface mesh resolution was varied, while the underlying volumetric mesh topology remained unchanged.

2.4. Beamforming reference

Conventional delay-and-sum beamforming was performed with Acoular [5], [6] using a virtual planar Vogel array of 151 microphones. As the comparison is presented at 2 kHz, the array diameter D and microphone distance z were both set to 1.0 m ($D/z = 1$), providing sufficient aperture relative to the acoustic wavelength. Cross-spectral matrices were obtained by Welch averaging of microphone pressures synthesised with FWH-next from the LES surface pressure in each one-third-octave band. The CFD surface mesh served

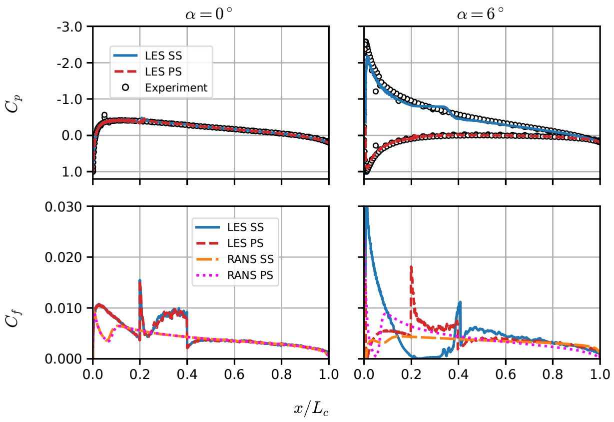

Figure 1: Pressure coefficient C_p (LES vs. experiment) and skin-friction coefficient C_f (LES vs. RANS) at $\alpha = 0°$ and $6°$, suction side (SS) and pressure side (PS).

as the steering grid, yielding source distributions at identical surface points. Since both methods use the same LES surface pressure as input, the comparison evaluates the consistency of the two localization operators rather than providing an independent reference.

3. Results

3.1. Aerodynamic and acoustic validation

Before the source-localization analysis, the solution was validated against RANS predictions [9] and experiment [11] through the pressure coefficient C_p, the skin-friction coefficient C_f, the wall-pressure spectrum and the far-field spectrum. Results for the 0.25 mm mesh, which agreed best with the reference data, are shown.

Fig. 1 compares the LES C_p with experiment and C_f with fully turbulent RANS. In the LES an explicit

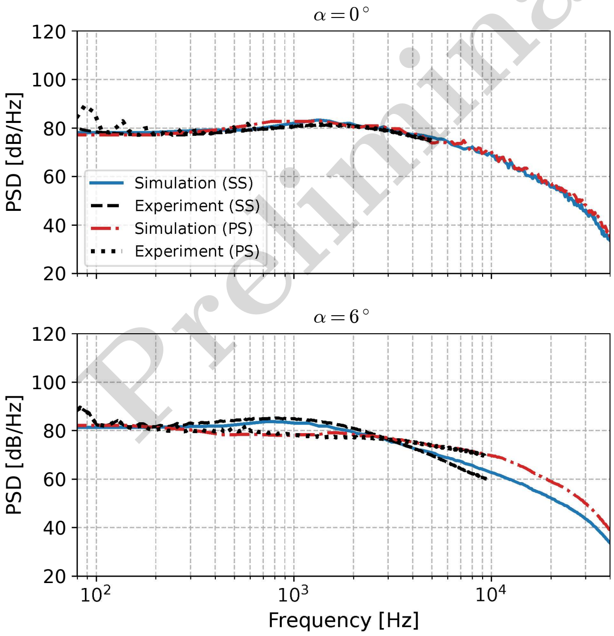

Figure 2: Wall-pressure spectrum near the trailing edge: LES vs. experiment at $\alpha = 0°$ and $6°$ on the suction (SS) and pressure (PS) sides.

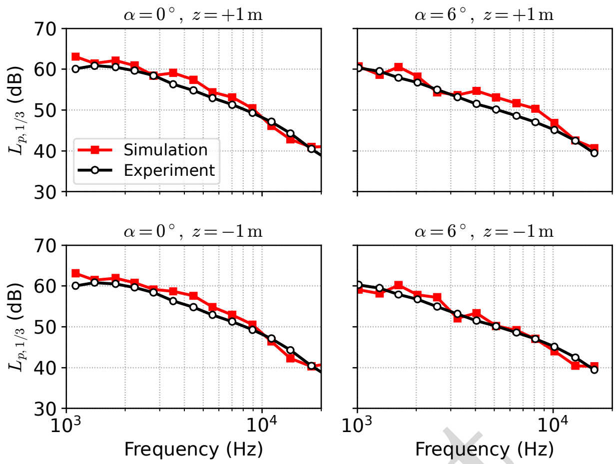

Figure 3: One-third-octave far-field spectra at observer angles $\pm 90°$, 1.0 m from the airfoil, for $\alpha = 0°$ and $6°$: LES vs. experiment.

(artificial roughness) tripping was applied in the area 20% to 40% of the chord for both AoAs. This is seen in the sudden changes in the C_f values. While the flow stays attached at $\alpha = 0°$, the suction side at $\alpha = 6°$ shows a separation bubble, indicated by vanishing C_f values and a corresponding plateau in the C_p distribution. Other than that at both angles of attack the surface pressure distributions agree well with the measurements and the C_f values agree with the RANS distribution downstream of about half the chord, i.e. in the area of interest. The near-trailing-edge wall-pressure spectrum (Fig. 2) reproduces the measured levels and spectral shape on both the suction (SS) and pressure (PS) sides, confirming that the LES captures the unsteady loading that drives the radiated sound. A 2D–3D correction [13] was applied to the numerical far-field spectra for comparison with the measurements. Consistently, the one-third-octave far-field spectra (Fig. 3) match the measurements to within about 1–2 dB, with a slight mid-frequency over-prediction at 6°.

The effect of surface resolution on the reconstructed far field was then assessed for $\alpha = 0°$. The complex surface pressure of each mesh (1.0, 0.5, 0.25 mm)

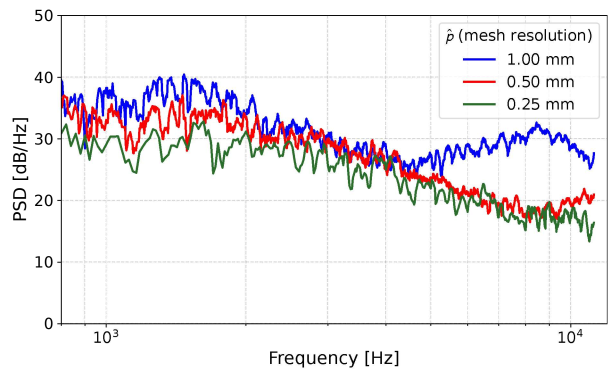

Figure 4: FW-H far-field spectra reconstructed from the surface pressure for three surface resolutions ($\alpha = 0°$, observer 20 m, 90°).

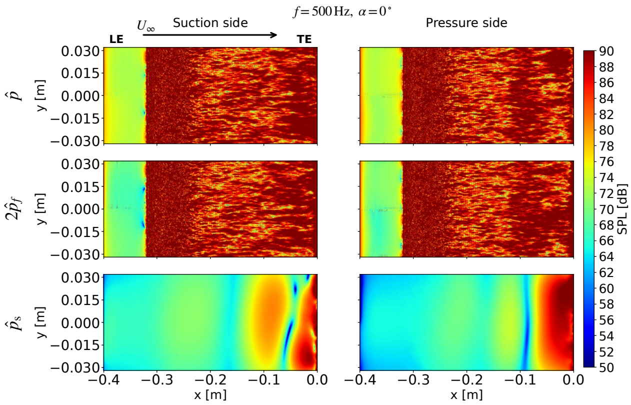

(a) $\alpha = 0°$, 500 Hz

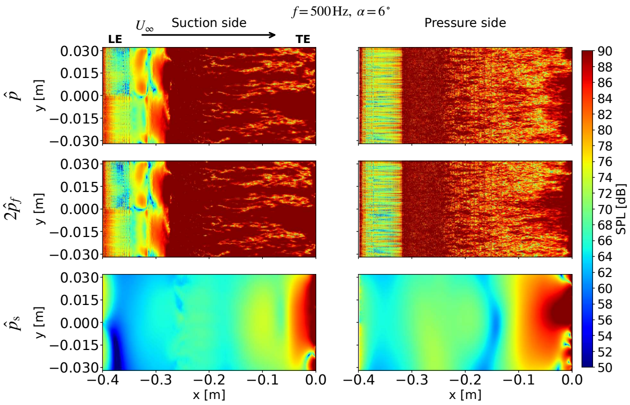

(b) $\alpha = 6°$, 500 Hz

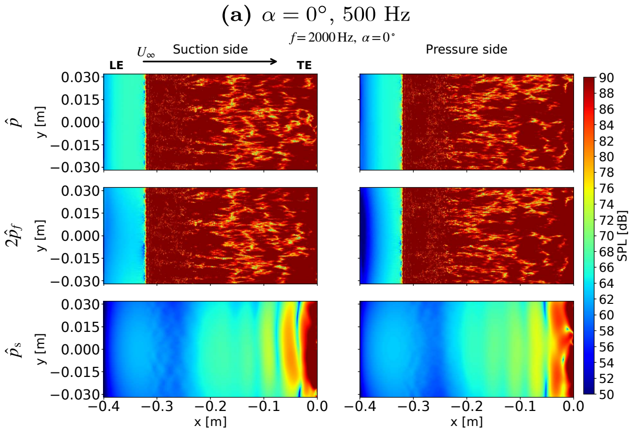

(c) $\alpha = 0°$, 2000 Hz

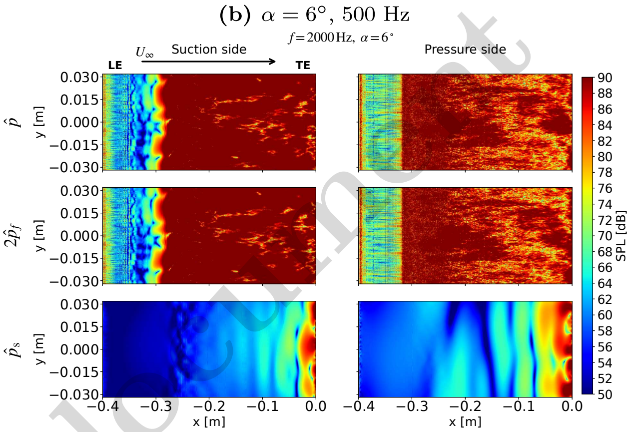

(d) $\alpha = 6°$, 2000 Hz

Figure 5: Comparison of the total surface pressure $\hat{p}$, free-field pressure $2\hat{p}_\mathrm{f}$, and acoustically active surface pressure $\hat{p}_\mathrm{S}$ for the NACA0012 airfoil at $\alpha = 0°$ and $6°$ in the 500 Hz and 2000 Hz third-octave bands.

was propagated with the FW-H formulation to an observer 20 m from the airfoil at about 90°; the resulting spectra are compared in Fig. 4. The 0.5 and 0.25 mm meshes agree up to progressively higher frequencies, whereas the 1.0 mm mesh shows spurious high-frequency content associated with the under-resolved surface pressure. The 0.25 mm mesh was therefore selected for all subsequent analyses.

3.2. Surface source reconstruction

The diffraction filter was applied to the 0.25 mm mesh at $\alpha = 0°$ and $6°$. Two one-third-octave bands, 500 Hz and 2000 Hz, are examined to probe the filter at low and high frequency. Figures 5c and 5d illustrate the decomposition of Eq. (3) at 2000 Hz: the free-field pressure $2\hat{p}_\mathrm{f}$ is almost indistinguishable from the total pressure $\hat{p}$, so that subtracting it isolates the acoustically active pressure $\hat{p}_\mathrm{S}$ and removes the non-radiating hydrodynamic contribution. As a result the trailing edge shines up as the source of sound as expected. Figures 5a and 5b show the same for the low frequency of 500Hz, representing an acoustically compact case. In spite of the compactness the distribution of p_S clearly identifies the trailing edge as the source of sound. Since this compact case is most challenging it is appropriate to test the localization performance of the acoustically active pressure $\hat{p}_\mathrm{S}$ vs. the source quantity $\hat{q}_\mathrm{S}$. As clearly observable in Figures 6a and 6b $\hat{q}_\mathrm{S}$ shows a more clear picture. All distributions appear somewhat inhomogeneous along the span; for extremely long simulation times this effect would vanish according to improved statistics. To quantify these distributions, a spanwise RMS average was computed along the surface. Figures 7 and 8 show the results at 500 Hz and 2000 Hz for both angles of attack. The total and free-field pressures remain dominated by the hydrodynamic field and vary smoothly, without isolating any source regions, whereas $\hat{p}_\mathrm{S}$ and $\hat{q}_\mathrm{S}$ exhibit pronounced maxima at the trailing edge. Interestingly, only for the 500 Hz case and at $\alpha = 6°$ (Fig. 7) the source quantities indicate some source activity at the leading edge as well. This is attributed to the fact that there is turbulent flow around the leading edge, which significantly diffracts large scale (low frequency) surface pressure, thus producing sound. For 2000 Hz no leading edge source is observed because the curvature radius appears large with respect to small scale pressure fluctuations; so diffraction related sound generation is weak.

3.3. Comparison with beamforming

Applying the filter a second time (Eq. 5) yields the surface source quantity $\hat{q}_\mathrm{S}$. Figures 6c and 6d compare the reconstructed $\hat{q}_\mathrm{S}$ map at $\alpha = 0°$, 2000 Hz, with

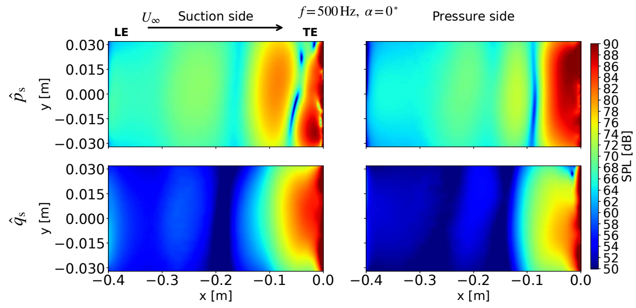

(a) $\alpha = 0°$, 500 Hz

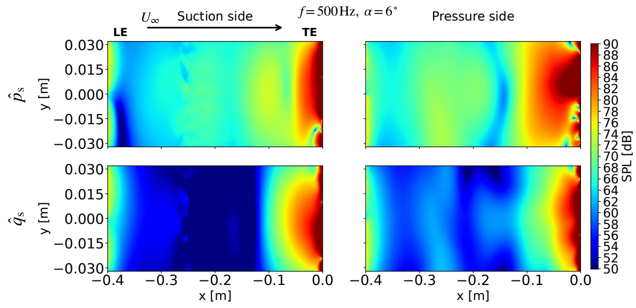

(b) $\alpha = 6°$, 500 Hz

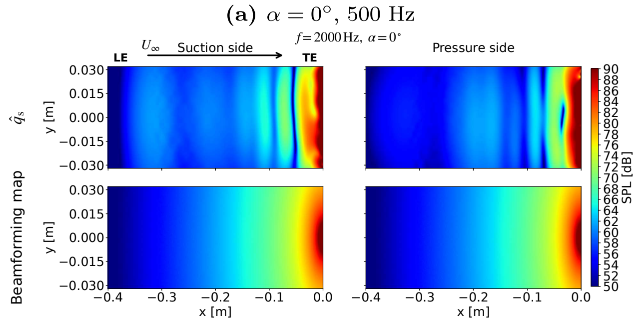

(c) $\alpha = 0°$, 2000 Hz

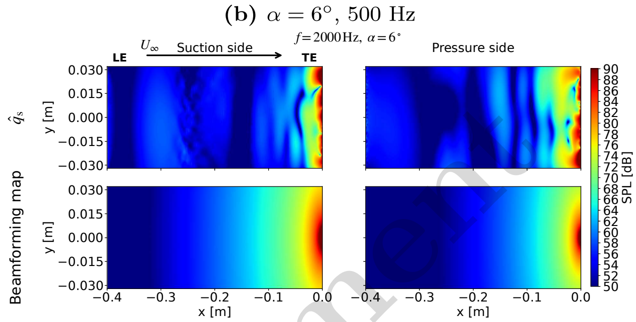

(d) $\alpha = 6°$, 2000 Hz

Figure 6: Comparison of source localization. Top figures: localization performance of $\hat{p}_s$ vs. $\hat{q}_s$ for the acoustically compact third octave band 500Hz. Bottom figures: reconstructed surface source quantity $\hat{q}_s$ with conventional delay-and-sum beamforming at 2000 Hz third-octave band. Evaluations performed on the identical CFD surface for the NACA0012 airfoil at $\alpha = 0°$ and $6°$.

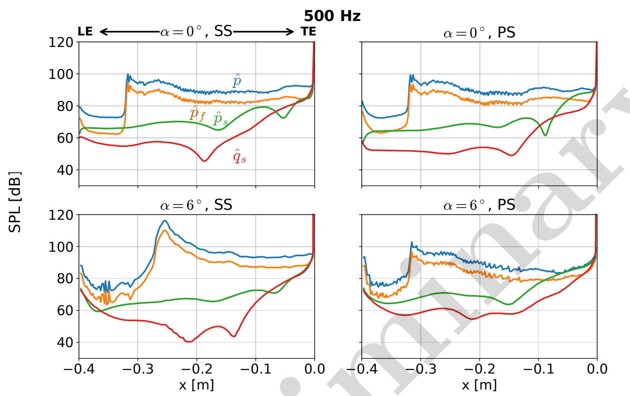

Figure 7: Spanwise-averaged surface pressure components at 500 Hz for $\alpha = 0°$ and $6°$, suction and pressure sides.

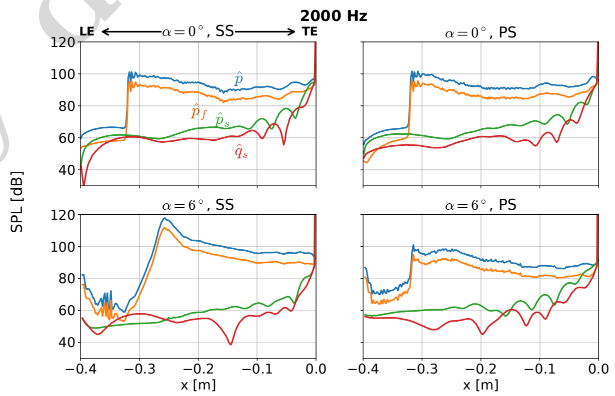

Figure 8: Spanwise-averaged surface pressure components at 2000 Hz for $\alpha = 0°$ and $6°$, suction and pressure sides.

the corresponding delay-and-sum beamforming map on the identical CFD surface. Both methods localize the trailing edge as the dominant source, but the diffraction filter is able to resolve substantially finer detail because $\hat{q}_S$ is evaluated based on vortical scales, whereas the beamforming map shows the characteristic aperture-limited broadening of the related array point-spread function inherently related to acoustic scales.

Consistent with earlier observations, the source distributions indicate somewhat reduced sound generation for the lifting airfoil at $\alpha = 6°$ compared to $\alpha = 0°$. This is attributed to the boundary layer thicknesses along with turbulence kinetic energy both being reduced at the pressure side while appearing increased on the suction side. As opposed to the (symmetric) non-lifting airfoil where suction and pressure side contribute equally to the overall acoustic spectrum for $\alpha = 6°$ the turbulence from the suction (pressure) side generates acoustic signals with lower(higher) frequency amplitude. As a consequence of the superposition of the effect of both sides the overall spectrum is wider but lower in amplitude for a given frequency when compared to the non-lifting (symmetric) case.

Relative to $\hat{p}$, the filtering of Eqs. (4) and (5) reduces the surface field over the quasi-planar part of the airfoil by up to about 30 dB at 2000 Hz and about 20 dB at 500 Hz, suppressing the non-radiating fluctu-

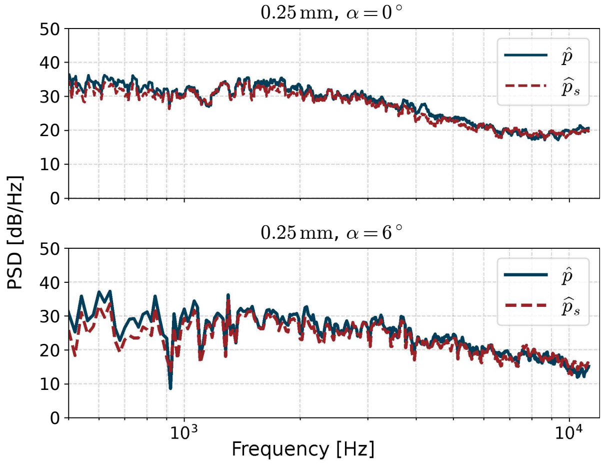

Figure 9: Far-field spectra reconstructed from the total pressure $\hat{p}$ and the active pressure $\hat{p}_S$ for both angles of attack (observer 20 m, 90°).

ations while retaining the localized source information. Finally, $\hat{p}$ and $\hat{p}_S$ for both angles of attack were propagated to the 20 m, 90° observer (Fig. 9). The two far-field spectra agree to within about 1–2 dB across the whole range, even though the underlying surface fields differ by roughly 40 dB. This confirms that the hydrodynamic fluctuations removed by the filter contribute negligibly to the radiated sound, while $\hat{p}_S$ seemingly retains all the source information.

4. Conclusions

A diffraction-filtering approach for aeroacoustic source localization was implemented in a frequency-domain FW-H framework and applied to WMLES of a NACA0012 airfoil at 0° and 6°. The filter suppresses the non-radiating part of the surface pressure by up to about 40 dB while leaving the far-field spectrum essentially unchanged, demonstrating that the removed components do not radiate. The reconstructed source quantity $\hat{q}_S$ localizes the trailing edge as the dominant source and, being evaluated directly on the CFD surface, resolves finer spatial detail than delay-and-sum beamforming while agreeing with it on the dominant source location. Moreover, the analysis shows that for low frequencies at an angle of attack there may occur some source activity at the leading edge as well. These results establish diffraction filtering as an efficient post-processing tool for extracting and localizing acoustically active regions directly from CFD surface pressure data. Future work will address a fully independent experimental reference and extension to higher frequencies and more complex geometries.

5. Acknowledgements

The authors thank Dr. Alexandre Suryadi and Dr. Christina Appel for providing the numerical mesh setup and RANS data used in this study, and Dr. Michael Mößner for providing the in-house FW-H solver FWH-next used throughout this work. Scientific support and access to the HPC system CARO provided by the German Aerospace Center (DLR) are also gratefully acknowledged. The HPC system CARO is partially funded by the Ministry of Science and Culture of Lower Saxony and the Federal Ministry of Research, Technology and Space.

References

[1] J. W. Delfs et al., "A quantity to identify turbulence related sound generation on surfaces," *Journal of Sound and Vibration*, 2024.

[2] J. W. Delfs et al., "Airframe noise source localization on the basis of surface pressure," in *AIAA AVIATION Forum*, 2025.

[3] J. Kreuzinger et al., "Quantitative Analyse der Schallleistung an Tragflügeln mit und ohne poröse Hinterkante," in *Proceedings of the DAGA 2024 Conference*, 2024.

[4] J. Kreuzinger et al., "CFD-CAA simulation of geometrically resolved porous trailing edge," in *Proceedings of the DAGA 2025 Conference*, 2025.

[5] E. Sarradj et al., "A python framework for microphone array data processing," *Applied Acoustics*, vol. 116, pp. 50–58, 2017.

[6] E. Sarradj et al., *Acoular – acoustic testing and source mapping software*, 2020.

[7] J. E. Ffowcs Williams et al., "Sound generation by turbulence and surfaces in arbitrary motion," *Philosophical Transactions of the Royal Society A*, vol. 264, no. 1151, pp. 321–342, 1969.

[8] R. Merino-Martínez et al., "A review of acoustic imaging methods using phased microphone arrays," *CEAS Aeronautical Journal*, vol. 10, pp. 197–230, 2019.

[9] M. Herr et al., "Benchmarking of trailing-edge noise computations—outcome of the BANC-II workshop," in *19th AIAA/CEAS Aeroacoustics Conference*. 2013.

[10] M. Herr et al., "Broadband trailing-edge noise predictions—overview of BANC-III results," in *21st AIAA/CEAS Aeroacoustics Conference*. 2015.

[11] R. Ewert et al., "RANS/CAA based prediction of NACA 0012 broadband trailing edge noise and experimental validation," in *Proc. 15th AIAA/CEAS Aeroacoustics Conference*, AIAA Paper 2009-3199, Miami, Florida, USA, May 2009.

[12] R. Ewert et al., "Hydrodynamic/acoustic splitting approach with flow-acoustic feedback for universal subsonic noise computation," *Journal of Computational Physics*, 2021.

[13] M. Soni et al., "Towards wall-modeled les with lattice boltzmann method for aeroacoustics: Application and understanding," in *28th AIAA/CEAS Aeroacoustics 2022 Conference*, 2022, p. 2918.